THE JOURNAL OF CHEMICAL PHYSICS **139**, 144701 (2013)

On the molecular origin of high-pressure effects in nanoconfinement: The role of surface chemistry and roughness

Yun Long (龙云),[1,a)] Jeremy C. Palmer,[1,b)] Benoit Coasne,[2,c)] Małgorzata Śliwinska-Bartkowiak,[3] George Jackson,[4] Erich A. Müller,[4] and Keith E. Gubbins[1,d)]

[1]*Department of Chemical and Biomolecular Engineering, North Carolina State University, Raleigh, North Carolina 27695-7905, USA*
[2]*Institut Charles Gerhardt Montpellier, Université de Montpellier 2 and CNRS (UMR 5253), Montpellier 34296, France*
[3]*Faculty of Physics, Adam Mickiewicz University, Poznan 61-614, Poland*
[4]*Department of Chemical Engineering, Imperial College London, South Kensington Campus, London SW7 2AZ, United Kingdom*

(Received 27 June 2013; accepted 19 September 2013; published online 10 October 2013)

Experiments and simulations both suggest that the pressure experienced by an adsorbed phase confined within a carbon nanoporous material can be several orders of magnitude larger than the bulk phase pressure in equilibrium with the system. To investigate this pressure enhancement, we report a molecular-simulation study of the pressure tensor of argon confined in slit-shaped nanopores with walls of various models, including carbon and silica materials. We show that the pressure is strongly enhanced by confinement, arising from the effect of strongly attractive wall forces; confinement within purely repulsive walls does not lead to such enhanced pressures. Simulations with both the Lennard-Jones and Barker-Fisher-Watts intermolecular potentials for argon-argon interactions give rise to similar results. We also show that an increase in the wall roughness significantly decreases the in-pore pressure due to its influence on the structure of the adsorbate. Finally, we demonstrate that the pressures calculated from the mechanical (direct pressure tensor calculations) and the thermodynamic (volume perturbation method) routes yield almost identical results, suggesting that both methods can be used to calculate the local pressure tensor components in the case of these planar geometries. © *2013 AIP Publishing LLC*. [http://dx.doi.org/10.1063/1.4824125]

I. INTRODUCTION

Phases confined in nanopores often exhibit a physical and chemical behavior that is significantly different from that of the bulk phase. Such effects arise from reduced dimensionality and from the strong interaction of the adsorbate molecules with the walls of the porous materials. These effects are relevant to applications such as the purification of water and air streams, heterogeneous catalysis, drug delivery, sensors, energy storage, the fabrication of nanomaterials such as nanowires, insulators in microcircuits, and electrodes for fuel cells and supercapacitors.

Experimental studies have shown that phenomena that occur in the bulk phase only at high-pressure (e.g., 10^3–10^4 bar or more) are often observed in nanopores in materials such as carbons and silicas, even though the bulk phase in equilibrium with the porous material is at a low pressure (1 bar or less). Examples include high-pressure chemical reactions, high-pressure solid phases, high-pressure effects in solid-liquid equilibriums, and effects on spectral properties.[1–7] The dimerization of nitric oxide, $2NO \rightleftharpoons (NO)_2$, has been well-studied and is a prototypical example of a high-pressure reaction that occurs in porous carbons at low pressure. In activated carbon fibers (with an average pore width of 0.8 nm), the mole fraction of dimers is found to be 99% at 300 K and 1 bar bulk pressure, as measured by magnetic susceptibility, while in the bulk gas phase at the same conditions the corresponding yield is less than 1 mol.% dimer.[3] Fourier transform infrared spectroscopy experiments on this reaction in single-walled carbon nanotubes (1.35 nm in diameter) at somewhat lower temperatures similarly indicated ∼100 mol.% conversion to dimers.[1] A simple thermodynamic calculation suggests that a bulk phase pressure between 12 000 and 15 000 bar is required to achieve a dimer conversion of 98–99 mol.% at these temperatures. In addition, phases that occur only at high-pressure in the bulk material are often observed in nanopores. High-resolution transmission electron microscopy and synchrotron X-ray diffraction experiments provided evidence that KI nanocrystals in single-walled carbon nanohorns (∼2 nm diameter) exhibit the super-high-pressure B2 structure at pressures lower than 1 bar, which is induced at pressures above 19 000 bar for bulk KI crystals.[7] Surface force apparatus experiments have been used to observe liquid-solid transitions of nanophases confined between mica surfaces for several substances at temperatures

a)Present address: Department of Chemical and Biomolecular Engineering, National University of Singapore, 117576 Singapore
b)Present address: Department of Chemical and Biological Engineering, Princeton University, Princeton, New Jersey 08544, USA
c)Present address: Department of Civil and Environmental Engineering, Massachusetts Institute of Technology, Cambridge, Massachusetts 02139-4307, USA
d)Author to whom correspondence should be addressed. Electronic mail: keg@ncsu.edu

well above their normal melting points, T_{mp}. For example, cyclohexane (T_{mp} = 279 K) freezes at 296 K and n-dodecane (T_{mp} = 263.4 K) freezes at 300 K when confined between mica surfaces in the surface force apparatus, while the bulk phases freeze at ~440 bar at 296 K[4–6] and ~1860 bar at 300 K,[2] respectively. Such a high-pressure effect on freezing of confined substances is consistent with recent molecular-simulation studies, in which in-pore freezing was found to be very sensitive to small increases in the bulk external pressure, which induced large pressure increases within the confined phase.[8] Finally, several experimental small-angle X-ray scattering studies suggest that there are significant effects of the adsorption of a confined phase on the pore width and interlayer atomic spacing of the pore walls, indicating a strong positive or negative pressure normal to the walls.[9–15]

The pressure tensor of argon adsorbed in a slit carbon pore has been studied by molecular simulation.[15,16] The pressure tensor **P** was calculated using the mechanical route with the Irving-Kirkwood (IK) definition of **P**[17,18] for the central region for a finite pore. In this study, we expand these results and report molecular-simulation results for the pressure tensor of a fluid of spherical molecules (argon) confined within a slit pore with wall strengths characteristic of a variety of materials, including carbons and silicas. We explore the effects of the structure of the wall and of the adsorbate-adsorbate and adsorbate-wall forces on the pressure enhancement, and demonstrate that it is the attractive interaction between the adsorbate molecules and the pore walls that is the major factor that determines the pressure enhancement. The large pressures found in the confined systems are strongly influenced by the bulk gas pressure and by the ability of the adsorbate to wet the pore walls. We also study the pressure and density of confined argon along the whole pore length and show how they change near the pore mouth.

II. PRESSURE TENSOR IN A SLIT PORE

The total pressure exerted on a system or an elementary surface area can be understood as the sum of a kinetic (ideal gas) contribution from the convective momentum transport of molecules and a configurational contribution due to interactions among molecules. For an inhomogeneous fluid the pressure is a second-order tensor **P**, where the component $P_{\alpha\beta}$ gives the force per unit area in the β-direction on a surface pointing in the α-direction.[18]

In the case of a fluid confined within a slit pore at equilibrium, the axial symmetry about the z-axis (normal to the pore walls) and translational symmetry in the xy-plane imply that all the off-diagonal components are zero, and there are only two independent, non-zero components: $P_{xx} = P_{yy} = P_T$, the tangential pressure (parallel to the wall); and $P_{zz} = P_N$, the pressure normal to the wall; moreover, they are only functions of the z-coordinate[18] (except near the pore mouth),

$$\mathbf{P} = \mathbf{P}_{kin} + \mathbf{P}_{conf} = \begin{bmatrix} P_{xx} & P_{xy} & P_{xz} \\ P_{yx} & P_{yy} & P_{yz} \\ P_{zx} & P_{zy} & P_{zz} \end{bmatrix} \overset{\text{slitpore}}{=} \begin{bmatrix} P_T(z) & 0 & 0 \\ 0 & P_T(z) & 0 \\ 0 & 0 & P_N(z) \end{bmatrix}. \quad (1)$$

If the pore walls are treated atomistically and there is no external field, the condition of mechanical equilibrium (no net momentum transport between bulk and confined phases) is $\nabla \bullet \mathbf{P} = 0$. This condition will be satisfied if there is physical contact between the confined phase and the bulk phase that is in thermodynamic equilibrium with it. For the slit pore system, mechanical equilibrium requires that P_N be a constant within the pore, i.e., independent of x, y, and z.[18]

The kinetic contribution of the local pressure tensor in a slit pore is well defined and is $\mathbf{P}_{kin}(z) = \rho(z) k_B T \mathbf{1}$, where $\rho(z)$ is the local number density of the molecules, k_B is Boltzmann constant, T is temperature, and **1** is the unit tensor. However, the configurational contribution to the local pressure tensor is not uniquely defined, and it is necessary to adopt an operational definition of how the intermolecular pair forces contribute to the pressure at a point in space, as discussed below.[17–19]

A. Irving-Kirkwood definition

The pressure tensor can be calculated by the mechanical route according to the momentum conservation law. For fluids composed of spherical molecules, interacting through a pairwise additive potential, the local pressure tensor can be expressed as[18,20]

$$\mathbf{P}(\mathbf{r}) = \rho(\mathbf{r}) k_B T \mathbf{1} - \frac{1}{2} \left\langle \sum_{i \neq j} \frac{\partial u(ij)}{\partial \mathbf{r}_{ij}} \int_{C_{ij}} d\tilde{l} \delta(\mathbf{r} - \tilde{l}) \right\rangle, \quad (2)$$

where **r** is the position vector, i and j are indices of molecules, $u(ij)$ is the pair potential between molecules i and j, C_{ij} is any arbitrary contour connecting the center of mass of molecule i, $\mathbf{r}_i$, to the center of mass of molecule j, $\mathbf{r}_j$, $\mathbf{r}_{ij} = \mathbf{r}_j - \mathbf{r}_i$, and $\delta(x)$ is the Dirac delta function. The second term on the right-hand side in Eq. (2) is the configurational contribution to the pressure tensor, and for an inhomogeneous system, different choices of the contour C_{ij} will lead to different definitions of the local pressure tensor, the most widely used definitions being those of Irving-Kirkwood and Harasima.

Irving and Kirkwood[17] chose C_{ij} to be a straight line connecting the centers of molecules i and j. In the planar case, the Irving-Kirkwood expression for the pressure can be written as[21]

$$P_{\alpha\alpha,IK}(z_k) = \rho(z_k) k_B T \mathbf{1} - \frac{1}{2A} \left\langle \sum_{i \neq j} \frac{(\mathbf{r}_{ij})_\alpha (\mathbf{r}_{ij})_\alpha}{r_{ij}} \frac{u'(r_{ij})}{|z_{ij}|} \times \theta\left(\frac{z_k - z_i}{z_{ij}}\right) \theta\left(\frac{z_j - z_k}{z_{ij}}\right) \right\rangle, \quad (3)$$

where $u'(r_{ij}) = du/dr_{ij}$, z_k is the z-coordinate for the plane where the pressure tensor is evaluated, α represents the x-, y-, or z-directions, $\theta(x)$ is the Heaviside step function, and A is the area of the z-plane. The two Heaviside step functions in Eq. (3) ensure that the interaction between molecules i and j contributes to the pressure tensor at plane $z = z_k$ if the straight line between molecules i and j passes through that plane. The tangential and normal components of the pressure tensor for

planar surface can be written as[21]

$$P_{T,IK}(z_k) = \rho(z_k)k_BT - \frac{1}{4A}\left\langle \sum_{i\neq j} \frac{x_{ij}^2 + y_{ij}^2}{r_{ij}} \frac{u'(r_{ij})}{|z_{ij}|} \times \theta\left(\frac{z_k - z_i}{z_{ij}}\right)\theta\left(\frac{z_j - z_k}{z_{ij}}\right)\right\rangle, \quad (4)$$

$$P_{N,IK}(z_k) = \rho(z_k)k_BT - \frac{1}{2A}\left\langle \sum_{i\neq j} \frac{z_{ij}^2}{r_{ij}} \frac{u'(r_{ij})}{|z_{ij}|}\theta\left(\frac{z_k - z_i}{z_{ij}}\right)\theta\left(\frac{z_j - z_k}{z_{ij}}\right)\right\rangle. \quad (5)$$

Equations (4) and (5) are convenient for computer coding.

B. Harasima definition

Harasima[22] chose the contour C_{ij} to be composed of two straight segments: from (x_i, y_i, z_i) to (x_j, y_j, z_i), and then from (x_j, y_j, z_i) to (x_j, y_j, z_j). In the case of the planar surface, the Harasima normal component of the pressure tensor is the same as that for the Irving-Kirkwood definition, and the tangential component can be written as[21]

$$P_{T,H}(z_k) = \rho(z_k)k_BT - \frac{1}{4A}\left\langle \sum_{i\neq j} \frac{{x_{ij}}^2 + {y_{ij}}^2}{r_{ij}} u'(r_{ij})\delta(z_k - z_i)\right\rangle. \quad (6)$$

The physical meaning of the Dirac delta function in Eq. (6) is that the configurational part of the tangential pressure is zero at a plane where there are no molecules. Thus, in a layering system, the Harasima tangential pressure is "concentrated" on the planes where the molecular layers are located, whereas the Irving-Kirwood tangential pressure is "distributed" along the space between the molecular layers.

C. Volume perturbation method

The pressure tensor can also be calculated from a direct thermodynamic definition. The pressure is given by the decrease in the Helmholtz free energy for an infinitesimal increase in the volume in the constant-*NVT* ensemble. We refer to this as the volume perturbation method (sometimes referred to as the ghost volume change method)[23–29] of pressure calculation. For a homogeneous phase the pressure can be obtained by[23–27,29–32]

$$P^V = -\left(\frac{\partial F}{\partial V}\right)_{N,T} = k_BT\left(\frac{\partial \ln Q(V)}{\partial V}\right)_{N,T}, \quad (7)$$

where F is the Helmholtz free energy, V is the volume of the system, N is the total number of the particles, and Q is the canonical partition function. For an inhomogeneous phase, if we change the volume by a small amount ΔV by perturbing in the α-direction only (keeping the other two dimensions, L_β, constant), the pressure tensor component $P_{\alpha\alpha}$ can be obtained as:[26,29]

$$P_{\alpha\alpha}^V = -\left(\frac{\partial F}{\partial V}\right)_{N,T,L_{\beta\neq\alpha}} \approx \rho k_BT - \frac{k_BT}{\Delta V}\ln\left\langle \exp\left(\frac{-\Delta U}{k_BT}\right)\right\rangle_{N,T,L_{\beta\neq\alpha}}. \quad (8)$$

In the slit pore, the normal pressure tensor is a constant, and can be calculated from Eq. (8) by taking $\alpha = z$. On the other hand, the tangential pressure, which depends on z, should be calculated locally. To apply Eq. (8) to calculate the local tangential pressure, one can divide the system into a number of thin slabs in the z-direction, whose position and thickness are z_k and δz, respectively. Thus, the local tangential pressure is[33–36]

$$P_T^V(z_k) = \rho(z_k)k_BT - \frac{k_BT}{\Delta V}\ln\left\langle \exp\left(\frac{-\Delta U(z_k)}{k_BT}\right)\right\rangle_{N,T,L_z}, \quad (9)$$

where $\Delta U(z_k)$ is the configurational energy change at slab k. In order to calculate $\Delta U(z_k)$ for a particular slab we must define how the pair potential energies will be assigned. Different choices will give different tangential pressure profiles, but their integrals over the pore width will be the same in the case of planar symmetry.[20] Two possible choices are: (1) if molecule i is located in slab k_i, and molecule j is located in slab k_j, then half of the interactive energy between them, 1/2 $u(r_{ij})$, contributes to slab k_i, and the other half, 1/2 $u(r_{ij})$, contributes to slab k_j; and (2) the interactive energy $u(r_{ij})$ linearly contributes to the slabs between them, i.e., each slab takes a fraction of $\delta z/|z_{ij}|$ $u(r_{ij})$. With both choices, the energy summation over all the slabs provides the same total energy for the pore system. The first choice was mathematically defined by Ladd and Woodcock:[37]

$$U(z_k) = \frac{1}{2}\sum_{i\neq j} H_k(z_i)u(r_{ij}),$$
$$\text{where } H_k(z_i) = \begin{cases} 1, & \text{for } |z_i - z_k| < \delta z/2 \\ 0, & \text{otherwise} \end{cases}. \quad (10)$$

The top-hat function H_k in Eq. (10) is analogous to the use of the Dirac delta in Eq. (6), corresponding to the Harasima definition used with the mechanical route. Thus, the local tangential pressure calculated with the assignment of energy defined by Eq. (10) should be equivalent to the Harasima pressure from the mechanical route. This definition was adopted by Ghoufi *et al.*[31] to calculate the surface tension of water in slit pores.

We also develop the mathematical expression for the second choice of energy assignment,

$$U(z_k) = \frac{1}{2}\sum_{i=1}^{N}\sum_{j\neq i}^{N} \frac{\delta z}{|z_{ij}|}u(r_{ij})\theta\left(\frac{z_k - z_i}{z_{ij}}\right)\theta\left(\frac{z_j - z_k}{z_{ij}}\right), \quad (11)$$

where θ is the Heaviside function. As with the Irving and Kirkwood partitioning (cf. Eq. (4)), the product of two θ functions ensures that the pair-wise interactive energy only contributes to slabs between the two molecules. Thus, the local tangential pressure calculated by this definition of energy

assignment (Eq. (11)) should be equivalent to the IK pressure calculated following the mechanical route.

III. SIMULATION DETAILS AND MODELS

We investigate the pressure tensor of argon (a) confined in various slit pore models. We consider a Lennard-Jones (LJ) model for argon, where $u_{aa}(r_{ij}) = 4\varepsilon_{aa}[\sigma_{aa}/r_{ij})^{12} - (\sigma_{aa}/r_{ij})^6]$, and $\sigma_{aa} = 0.3405$ nm, $\varepsilon_{aa}/k_B = 119.8$ K,[38] and a truncation of the potential at $5\sigma_{aa}$. The Barker-Fisher-Watts (BFW) potential model is also assessed, as it provides a more accurate representation of the argon-argon interaction,[39]

$$u_{aa}{}^{BFW}(r_{ij}) = \varepsilon_{BFW}\left\{\exp[\alpha(1-r_{ij}/r_m)]\sum_{i=0}^{5}A_i(r_{ij}/r_m-1)^i - \sum_{j=3}^{5}C_{2j}/[\delta+(r_{ij}/r_m)^{2j}]\right\},$$

$$u_{aa}{}^{/BFW}(r_{ij}) = \frac{\varepsilon_{BFW}}{r_m}\left\{\exp\left[\alpha\left(1-\frac{r_{ij}}{r_m}\right)\right] \times \sum_{i=0}^{5}A_i\left(\frac{r_{ij}}{r_m}-1\right)^i\left[\frac{i}{(r_{ij}/r_m-1)}-\alpha\right] - \frac{r_m}{r_{ij}}\sum_{j=3}^{5}\frac{2jC_{2j}}{[\delta+(r_{ij}/r_m)^{2j}]^2}\left(\frac{r_{ij}}{r_m}\right)^{2j}\right\}.$$

The parameters ε_{BFW}, r_m, A_i, C_{2j}, and δ are taken from Ref. 40 and listed in Table I. The interaction energy vs. the separation distance for these two models are plotted in Fig. 1.

For carbons, a simple slit pore model is Steele's (10,4,3) potential, which treats the walls as structureless, rigid, and of infinite dimension (cf. Fig. 2(a)). The interaction of an adsorbate molecule with the wall is given by Ref. 41,

$$u_{aw}(z) = 2\pi\varepsilon_{ac}\rho_w\Delta_w\sigma_{ac}^2\left[\frac{2}{5}\left(\frac{\sigma_{ac}}{z}\right)^{10} - \left(\frac{\sigma_{ac}}{z}\right)^4 - \left(\frac{\sigma_{ac}^4}{3\Delta_w(z+0.61\Delta_w)^3}\right)\right], \quad (12)$$

where ε_{ac} and σ_{ac} are LJ parameters for an adsorbate molecule interacting with a carbon atom in the wall,

TABLE I. The BFW parameters for argon.[40]

ε_{BFW}/k_B (K)	142.095
r_m (nm)	0.37612
A_0	0.277 83
A_1	− 4.504 31
A_2	− 8.331 215
A_3	− 25.2696
A_4	− 102.0195
A_5	− 113.25
C_6	1.107 27
C_8	0.169 713 25
C_{10}	0.013 611
α	12.5
δ	0.01

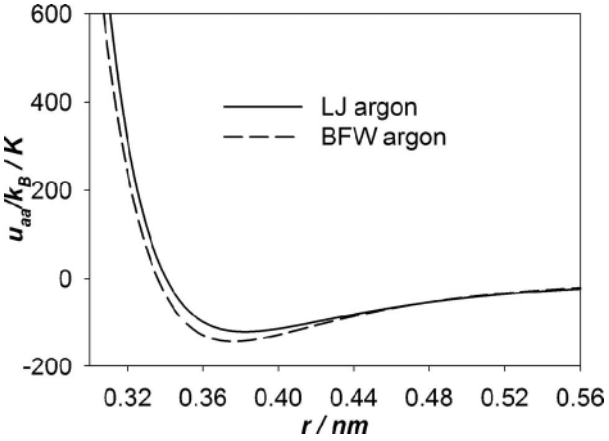

FIG. 1. Intermolecular interaction pair potentials for argon for the LJ and BFW models.

$\rho_w = 114$ nm^{-3} is the carbon atom density of the graphene wall, $\Delta_w = 0.335$ nm is the interlayer spacing between graphene sheets, and z is the distance between the center of an adsorbate molecule and the plane of the carbon atoms at the wall's surface.[41] Periodic boundary conditions are applied in the x- and y-directions, so that the slit pore is of infinite dimension in the xy-plane.

We also study a more realistic pore model with finite pore length and flexible and fully atomistic pore walls.[16] This model (shown in Fig. 2(b)) is a slit-shaped pore with 3 layers of graphene ($L_{x,wall} \times L_{y,wall} = 3.408$ nm $\times$ 6.8866 nm) in each wall. The pore is of finite length in the y direction, and so the confined phase is in direct physical contact with a bulk gas phase at both ends of the pore (each bulk phase has a y-length of 6.8866 nm, i.e., three times of the pore length). The two walls lie parallel to the xy-plane, and are symmetric about $z = 0$. The carbon atoms are connected to their lattice positions by springs, with the value of the spring constant, k_s, matching the adaptive intermolecular reactive bond order (AIREBO) potential,[42] a reactive force field for carbon; atoms in different layers interact via the LJ potential, where $\sigma_{cc} = 0.34$ nm and $\varepsilon_{cc}/k_B = 28$ K. The lattice positions of the carbon atoms in the outermost layers are fixed in space, but the lattice planes of the surface and central graphene layers are permitted to move, thus allowing the effect of the confined nanophase on the pore width and interlayer spacing of the pore wall to be studied. Periodic boundary conditions are applied in the x-direction only. In the y- and z-directions, hard wall boundary conditions are used. For the finite pore model (made of carbon as well as the silica pore described later), the properties are calculated in the region far away from the pore mouths (labeled "averaging region" with a length of 6 σ_{aa} in Figs. 2(b) and 2(c)), where the pore edge effects are negligible.

A variety of adsorbate-wall interactive potentials are used with the realistic pore model in order to understand the forces that lead to the pressure enhancement effects. In a first assessment, the fluid-wall interaction is modeled with a normal LJ potential characterized with the parameters defined earlier, and Lorentz-Berthelot combining rules are employed for the unlike pair interactions (i.e., $\varepsilon_{ac} = \sqrt{\varepsilon_{aa}\varepsilon_{cc}}$ and $\sigma_{ac} = (\sigma_{aa} + \sigma_{cc})/2$). The Weeks-Chandler-Andersen (WCA) purely

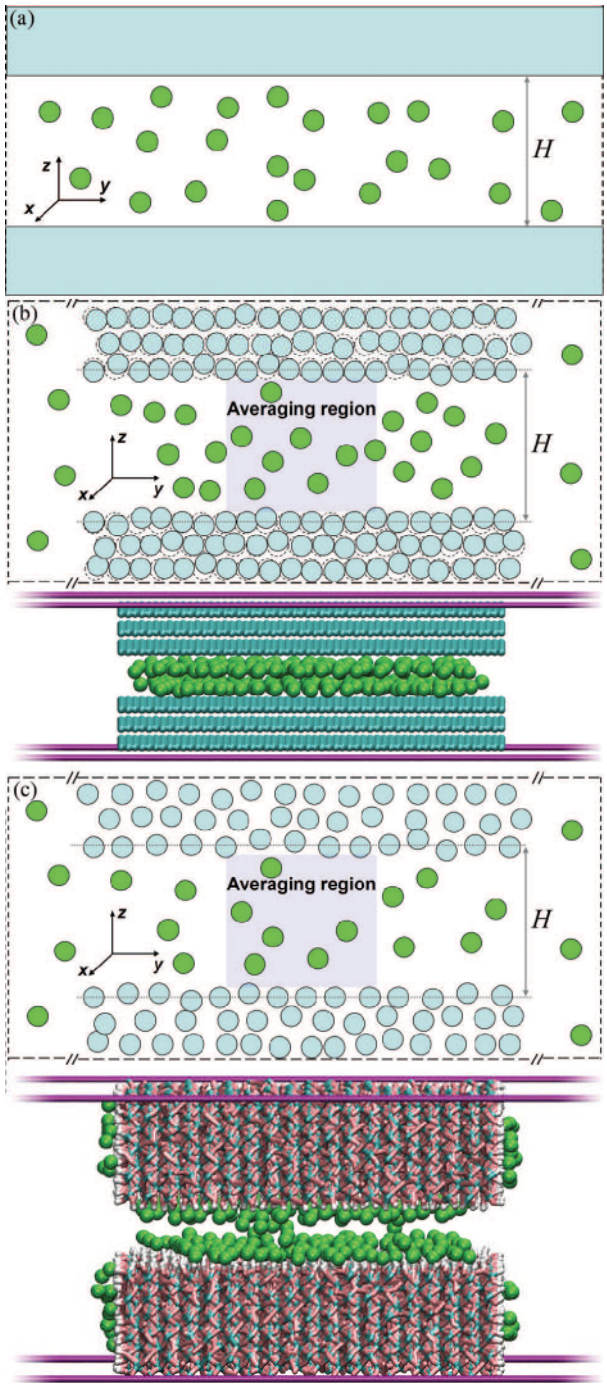

FIG. 2. The simulation cells of: (a) carbon slit pore described with a Steele (10,4,3) rigid, structureless wall; (b) carbon slit pore with atomistic, flexible wall; and (c) silica slit pore. The green circles represent adsorbed argon molecules, and the blue circles and slabs represent wall atoms and carbon structureless walls, respectively. Carbon atoms are shown at reduced scale for clarity. The atoms in silica are less dense than in the carbon wall.

repulsive potential[43] is then used for the fluid-wall interaction, with the LJ parameters of carbon as the wall parameters,

$$u_{ac}^{WCA}(r_{ij}) = \begin{cases} 4\varepsilon_{ac}[(\sigma_{ac}/r_{ij})^{12} - (\sigma_{ac}/r_{ij})^{6}] + \varepsilon_{ac} & r_{ij} < 2^{1/6}\sigma_{ac} \\ 0 & r_{ij} \geq 2^{1/6}\sigma_{ac} \end{cases}. \quad (13)$$

This potential model allows one to study whether the pressure enhancement arises from the attractive or repulsive adsorbate-wall forces, or from geometric confinement effects. In a subsequent investigation the fluid-wall interaction is modeled as a LJ potential, but the LJ parameter ε_{ww}/k_B between the wall atoms is varied from 0.982 K to 98.2 K, which allows the effect of the strength of the wall attraction (or the wetting parameter $\alpha_w = \rho_w \Delta_w \sigma_{aw}^2 \varepsilon_{aw}/\varepsilon_{aa}$) on the pressure enhancement to be studied.

Finally, we study the pressure tensor of argon in an atomistic finite silica slit pore (schematically shown in Fig. 2(c)). Starting with the β-cristobalite silica structure,[44] we carve out a slit-shaped pore, and remove the unsaturated Si atoms as well as the free oxygen atoms on the carved out surface. The dangling oxygen atoms (those having only one bond with Si atoms) are saturated by adding H atoms to neutralize the surface. The system is then randomized slightly. The model is now an atomistic silica pore with a finite length of 6.8 nm, and the bulk phase is in contact with each end of the pores. The fluid-wall interaction is modeled by the PN-TrAZ potential[45] with the parameters listed in Ref. 46.

We study argon adsorption in the aforementioned models for different bulk pressures. The reduced slit pore width ($H^* = H/\sigma_{aa}$) is varied from 2.0 to 8.0, where H is defined as the distance between the wall planes in the case of the Steele (10,4,3) potential, or the distance between the innermost graphene layers on opposing wall surfaces, when at their equilibrium positions (for the atomistic, flexible carbon model), or the average distance between oxygen layers on the opposing wall surfaces (for the silica slit pore). Semi-grand canonical Monte Carlo simulations are employed with fixed volume V, temperature T, chemical potential of the confined adsorbate μ_a, and number of wall atoms N_w (for the atomistic models). The system is first brought to thermodynamic and mechanical equilibrium for 10^8 Monte Carlo moves, and subsequently carry out a further 10^8 Monte Carlo moves to calculate the average properties (the same frequency is assigned to the translational insertion and deletion moves of adsorbate molecule as well as the translational move of wall atoms; the displacement of the lattice plane of the graphene layer is tried each 10 above-mentioned MC moves for the realistic pore wall model). To calculate the average in-pore density, the accessible pore width is used (the "dead" region due to the highly repulsive interaction between adsorbate and wall atoms is excluded); practically, the dead region can be determined from the space, close to the wall, with zero probability to find an adsorbate molecule, at a pressure higher than the condensation pressure.

IV. RESULTS AND DISCUSSION

A. Structureless rigid pore walls

For the simplest case, the density and pressure of LJ argon confined in a pore characterized with Steele's (10,4,3) structureless rigid infinite walls ($H^* = 3.0$) at 87.3 K are presented in Fig. 3. The argon density and pressure profiles at 1 bar bulk pressure are shown in Fig. 3(a). The two peaks in the density profile indicate the well-known layering effect in confined systems. More argon layers are found in larger

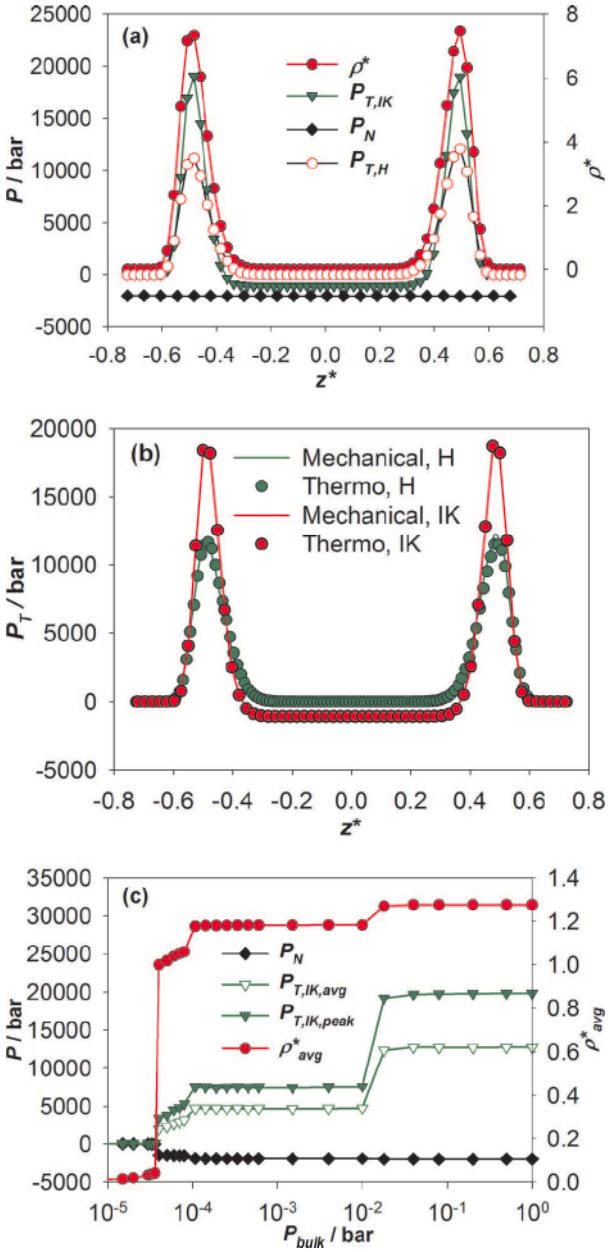

FIG. 3. Simulation results for a structureless rigid infinite slit pore (described with the Steele potential) of separation $H^* = 3.0$, at 87.3 K: (a) the density and pressure profiles at 1 bar bulk pressure; (b) the tangential pressure profiles from the mechanical route and thermodynamic route at 1 bar bulk pressure; and (c) the average in-pore density and pressures of argon as a function of bulk pressure.

pores, and the inner layers ($\rho^* = \rho\sigma_{aa}{}^3 < 5$ at the peak) are less dense than the layers in contact with the wall ($\rho^* > 7$ at the peak). From the simulation snapshots, it appears that the argon molecules in the contact layers adopt a face-centered cubic (fcc) structure, which only occurs at pressures higher than a few hundred bar for bulk argon at 87.3 K. The peak in the tangential pressure is located where the density peak occurs. The maximum tangential pressure is enhanced by a factor of ∼19 000 (as obtained with the IK definition) or ∼12 000 (with the Harasima definition), and the normal pressure, which is a constant through the pore width, is negative in this case and enhanced by a factor of ∼2000. The normal pressure can oscillate with pore width due to packing effects, with an amplitude of ∼5000 bar, and can be positive or negative.[16] In the central region of the pore (the vicinity of $z = 0$), where the density is close to zero (very low probability to find an argon molecule due to the layering effect), the Harasima tangential pressure is almost zero as expected, but the IK tangential pressure is negative with appreciable magnitude (−1000 bar), because the attractive interaction between argon layers contributes to the negative pressure at the planes sitting between the argon layers, i.e., in the central region. However, the integrals of the tangential pressures over the pore width (the difference from the normal pressure corresponding to the surface tension) obtained with both definitions are the same (within ∼0.1%). We also compare the pressures calculated with the thermodynamic route to those with the mechanical route, and find that the tangential pressure from the two routes agree within statistical error (Fig. 3(b)). Moreover, the normal pressure determined with these two routes is essentially the same (−2204 bar).

The effects of bulk pressure in a structureless rigid pore with periodic boundary conditions are shown in Fig. 3(c) for the pore of $H^* = 3.0$ at 87.3 K. Argon starts to be adsorbed at $P_{bulk} \sim 1 \times 10^{-5}$ bar, and at higher pressures two jumps in the density and $P_{T,IK,peak}$ correspond to phase transitions from a gas-like to a liquid-like phase (at $P_{bulk} \sim 5 \times 10^{-5}$ bar), and from the liquid-like to a fcc crystal phase (at $P_{bulk} \sim 1 \times 10^{-4}$ bar). After the transition to the fcc crystal phase, there is another jump in the density and tangential pressure (at $P_{bulk} \sim 1 \times 10^{-2}$ bar); by contrast, no such jump is observed for the atomistic flexible finite pore (Fig. 4(b)). This additional jump in a pore with fixed periodic boundary conditions occurs because the pore can only hold an integer number of molecules; more argon cannot adsorb until the bulk pressure (chemical potential) is large enough to squeeze an additional molecule into the adsorbed layer. By contrast, for a pore of finite length, the in-pore molecular arrangement and intermolecular distance can change gradually depending on the bulk pressure, since molecules can adsorb at the mouth and on the external surface of the pore. Thus, for a given bulk pressure the average density within the pore of finite length can be higher than for the rigid pore with periodic boundary conditions, and since the average separation distance between molecules is then smaller for the finite pore, the tangential pressure will be higher. These phenomena were also observed in a non-local density functional theory study of gas adsorption in finite and infinite carbon pores.[47] In addition to the maximum value, the average of the pressure across the pore, $P_{T,IK,avg} = \int_{-H/2}^{H/2} P_{T,IK}(z)\rho(z)dz / \int_{-H/2}^{H/2} \rho(z)dz$, is also shown in Fig. 3(c). Both increase rapidly with P_{bulk}, following the increase in density, while P_N is only slightly affected. The pressure enhancement factor, $P_{T,IK,peak}/P_{bulk}$, can be as large as 7 orders of magnitude at $P_{bulk} \sim 10^{-4}$ bar and 4 orders of magnitude at $P_{bulk} \sim 1$ bar at 87.3 K.

B. Atomistic flexible pore walls

In Fig. 4, we show results for the density and pressure of LJ argon confined in a more realistic slit pore model at

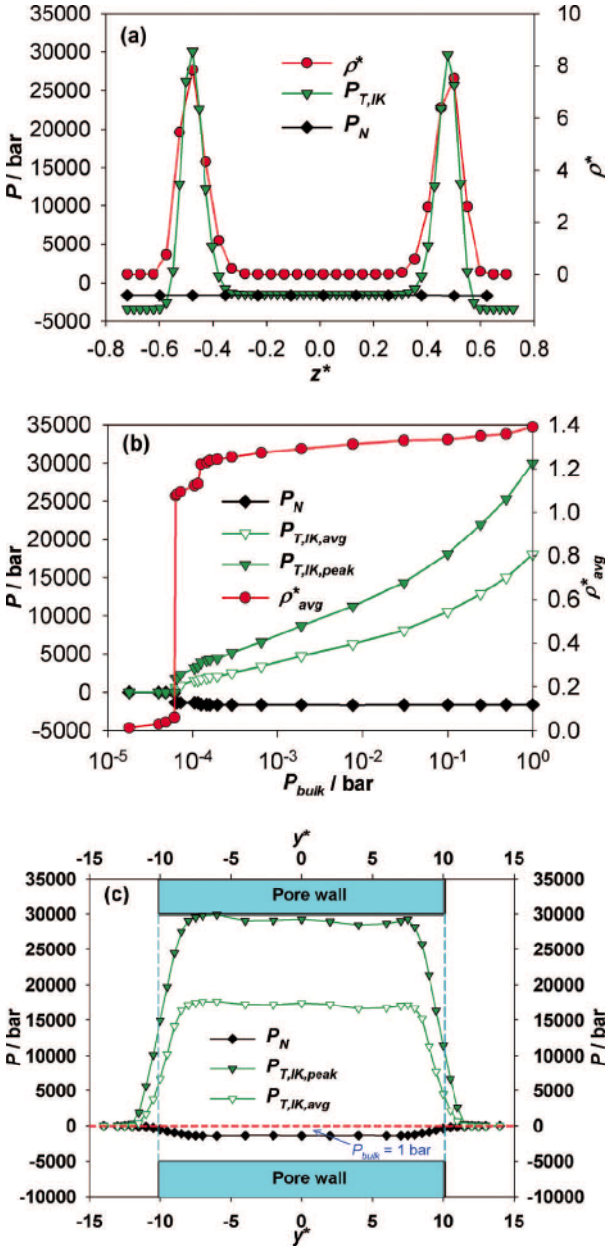

FIG. 4. The components of the pressure tensor for an atomistic flexible finite slit pore of $H_e^* = 3.0$, at 87.3 K: (a) the density and pressure profiles of LJ argon at 1 bar bulk pressure; (b) the average in-pore density and pressures of LJ argon as a function of bulk pressure; and (c) the pressures of LJ argon along the pore length, showing the behavior near the pore mouth, at 1 bar bulk pressure.

87.3 K: a fully atomistic flexible wall with finite length and of width $H_e^* = 3.0$, where H_e^* is the reduced pore width with respect to the argon diameter when the pore is empty, defined as the distance between the centers of the carbon atoms forming the first graphene layer on the opposing walls. In Fig. 4(a), we show the argon density and pressure profiles (in the central averaging region, hereafter, unless specified) at 1 bar bulk pressure. The results are quite similar to those obtained with the simpler Steele (10,4,3) structureless rigid wall model (Fig. 3(a)). The peak in the tangential pressure for the atomistic model is higher than for the simpler model (30 000 bar compared with 19 000 bar). A similar difference is also found for the peak in the density (8 compared with 6). This difference arises from the nature of the infinite rigid pore with periodic boundary conditions, where the argon layer is not as dense as it would be at the same bulk pressure in an infinitely long pore due to the reason discussed in Sec. IV A. The tangential pressure is then much lower because of the looser arrangement of argon. Hence, the slit pore of finite length gives a more realistic representation of the system. The normal pressure in this model is −1650 bar, in qualitative agreement with that found for the simpler model in Sec. IV A.

In Fig. 4(b), we show the effect of bulk pressure in the realistic model with a slit separation of $H_e^* = 3.0$ at 87.3 K. The bulk pressures at which argon starts to be adsorbed changes from a gas-like to a liquid-like phase, and then from the liquid-like to a fcc crystal phase as those in the simpler model (Fig. 3(c)). However, beyond these jumps, the isotherms in the realistic model change more smoothly than for the simpler model.

The finite atomistic pore model allows one to examine edge effects – how the pressure tensor components change in going from the pore center to its mouth. In Fig. 4(c), the pressures of LJ argon along the pore length at 87.3 K and 1 bar bulk pressure are shown. Both the normal and the tangential pressures are almost constant in the central region (in the y-direction) of the pore, and start to be less enhanced and approach to the bulk pressure when close to the pore mouth (starting at ∼2.0 σ_{aa} from the pore mouth).

C. Effect of the adsorbate interaction: BFW argon

The influence of the intermolecular potential model for argon (LJ vs. BFW) on the adsorption in slit pores is shown in Fig. 5 for the realistic finite pore model of width $H_e^* = 4.5$ at 87.3 K and 1 bar bulk pressure. The average in-pore densities of the two cases are almost the same (with ∼1% deviation), but while the LJ model argon exhibits a similar local density for the contact layer (∼9, peak value of reduced density) it has higher peak values for the central layers (∼6.4) than those for BFW model argon (5.5). The density peaks of the central layers for the BFW argon are slightly wider, and thus the central layer of BFW argon is slightly less closely packed than for LJ argon. For the contact layer, the calculated tangential pressure of the BFW argon (∼22 000 bar) is about the same as for the LJ argon (∼21 500 bar), while for the central layers it is appreciably higher for the BFW argon (∼6700 bar) than for LJ argon (∼5000 bar). This could be attributed to the configurational contribution from the interlayer interaction of argon: for BFW argon, which is softer, there is a higher probability to have argon molecules in different layers closer to each other compared with LJ argon, and this smaller separation distance gives rise to the repulsive contribution to the pressure tensor. From this observation, we conclude that the tangential pressure is not very sensitive to the potential model, because the resulting adsorbate arrangement will also contribute to the configurational pressure and compensate for small differences in the potential models.

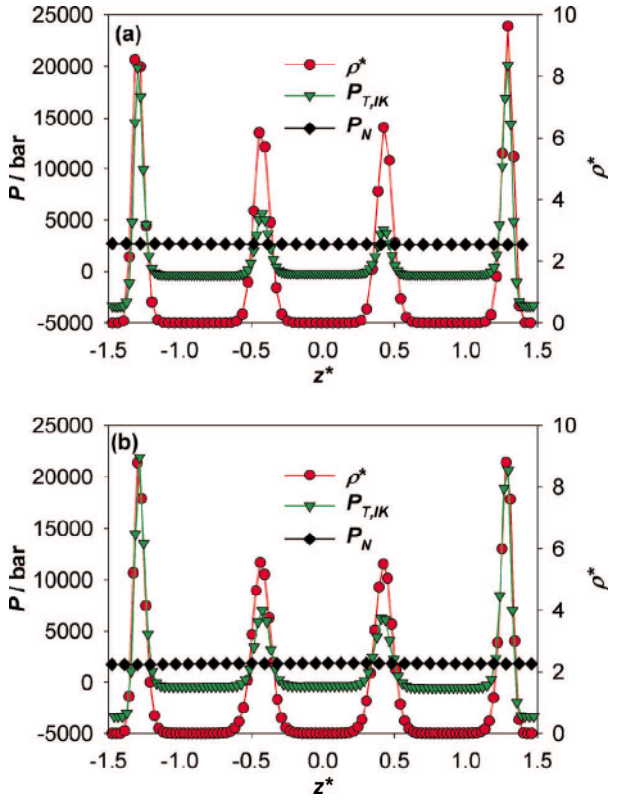

FIG. 5. The density and pressure profiles of (a) LJ argon and (b) BFW argon in an atomistic flexible finite slit pore of $H_e^* = 4.5$, at 87.3 K and 1 bar bulk pressure. The apparent drop in the normal pressure near the wall is believed to be an artifact due to poor statistics in this region.

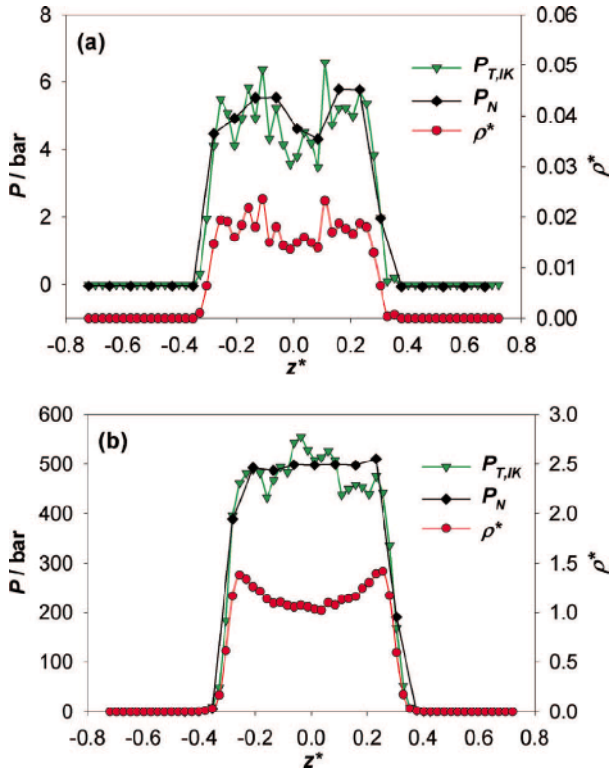

FIG. 6. The density and pressure profiles of argon in the atomistic flexible slit-pore model with finite length described using a WCA soft repulsive adsorbate-carbon potential, Eq. (13), at 87.3 K and a bulk pressure of (a) 5 bar and (b) 200 bar. The argon-argon interaction is the full Lennard-Jones potential, as before.

Furthermore, for a pore of $H_e^* = 4.5$, there are four argon layers and the interlayer spacing of argon is $\sim 0.85\,\sigma_{aa}$, smaller than the LJ diameter of argon, and thus the repulsive interaction of argon molecules in different layers is important. The normal pressure for BFW argon ($\sim$1790 bar) is appreciably smaller than that for LJ argon ($\sim$2660 bar), which is also a result of the softer nature of BFW argon (with the same degree of compression in the normal or z-direction, the repulsion between BFW argon is weaker than that for LJ argon). Therefore, LJ argon and BFW argon exhibit quantitatively similar layering and pressure enhancement phenomena, and thus the LJ potential model is a reasonable approximation with much higher efficiency in computation.

D. Effect of the argon-wall attractive interaction

An examination of the various contributions (kinetic, adsorbate-adsorbate, and adsorbate-wall interactions) to the enhanced tangential pressure in the argon layer in contact with the wall has indicated that the argon-argon configurational contribution is dominant at temperatures in the liquid range for all of the models studied. The in-plane radial distribution function also showed that the separation distance between argon molecules in this layer is reduced, so that the repulsive interaction is very strong.[16] To demonstrate the role of the attractive forces between the adsorbate molecules and the wall, we carry out simulations for the finite, atomistically structured wall for a WCA (purely repulsive) adsorbate-wall interaction, Eq. (13); the other (adsorbate-adsorbate, carbon-carbon) interactions remained the same as before. The resulting pressure and density profiles are shown in Fig. 6 for two different bulk pressures. At 5 bar bulk pressure, the density and the normal pressures are almost constant within statistical error. There is no layering, and the pressure is not enhanced (Fig. 6(a)). At 200 bar bulk pressure, there is a very weak layering effect, and the pressure is enhanced by a factor of $\sim$2.5 (Fig. 6(b)). This assessment indicates that the compression of the argon layers is mainly a result of the attractive forces exerted on them by the walls, and is not just a geometric confinement effect.

E. Effect of the wetting parameter

From the functional form of the Steele potential, one sees that the prefactor $\rho_w \Delta_w \sigma_{aw}^2 \varepsilon_{aw}$ governs the absolute strength of the solid-fluid interactions. Hence, it is useful to define a microscopic wetting parameter,[48,49] $\alpha_w = \rho_w \Delta_w \sigma_{aw}^2 \varepsilon_{aw}/\varepsilon_{aa}$, as the ratio of the effective average solid-fluid to fluid-fluid interaction strength.

The influence of α_w on the fluid density and pressure is studied by varying the parameter for the adsorbate-wall attraction (ε_{aw}). Walls with values of α_w much greater than 1 can be regarded as "strongly attractive," while those with α_w much less than 1 can be considered "weakly attractive." We show in

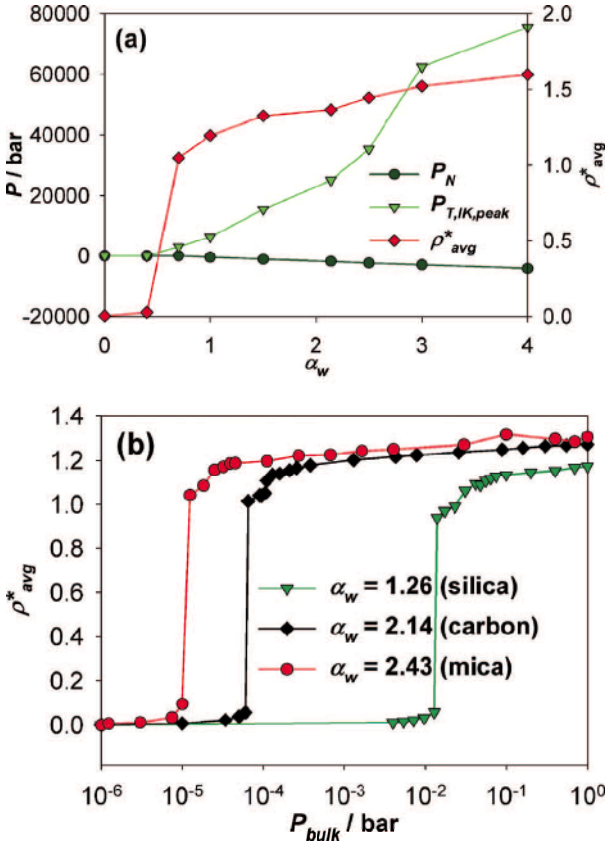

FIG. 7. The effect of the microscopic wetting parameter, α_w, for atomistic slit pores with finite length at 87.3 K and $H^*_e = 3.0$, on: (a) the in-pore average density, normal pressure, and maximum tangential pressure at 1 bar bulk pressure; and (b) the isotherm, for values of α_w corresponding to argon in silica, carbon, and mica slit pores.[41,49,50]

Fig. 7(a) the average in-pore density and maximum tangential pressure in pores of $H^*_e = 3.0$ with different α_w values. As expected, an increase in α_w raised the in-pore density and the argon phase is thus more closely packed. As the average interatomic distance becomes less than the value of σ, molecules explore the repulsive region of the intermolecular potential and the maximum tangential pressure increases accordingly. Additionally, as shown in Fig. 7(b), a larger value of α_w results in lower bulk pressure required for the phase transition, and a higher in-pore density. Here, we show the results for the pore walls with the α_w of 1.26, 2.14, and 2.43, which are comparable with the α_w of argon on silica, carbon, and mica surfaces, respectively,[41,49,50] while the atomistic structure of the wall is kept as graphene (we only change ε_{aw} to vary α_w).

F. LJ argon in large pores with atomistic flexible carbon walls

To explicitly illustrate the effects of increasing the pore width on the adsorption and the in-pore pressures, we performed simulations of LJ argon adsorption in carbon pores of $H^* = 15$ and 30 (5.1 and 10.2 nm) with atomistic flexible carbon walls, at 87.3 K and 1 bar bulk pressure. We also simulated the bulk LJ argon gas at the same temperature and bulk pressure (and thus the same chemical potential). The profiles

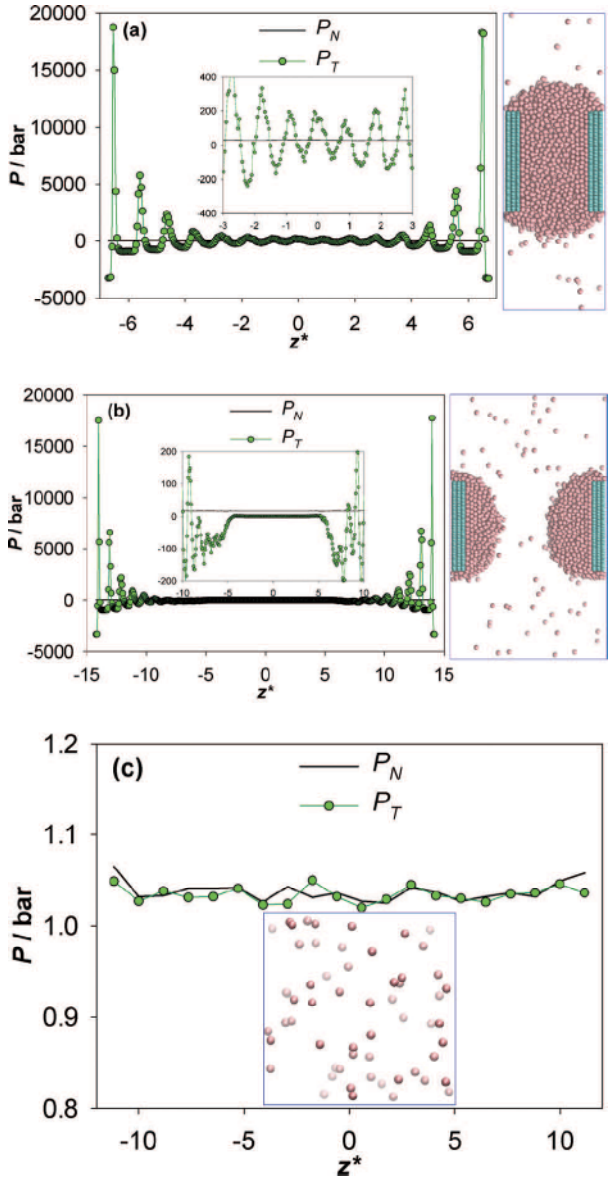

FIG. 8. Snapshots and tangential and normal pressure profiles of LJ argon confined in the atomistic flexible carbon slit pores at 87.3 K and 1 bar bulk pressure: (a) $H^* = 15$, (b) $H^* = 30$, and (c) without any confinement (bulk phase argon). In the snapshots, the dark blue rectangular (square) indicates the simulation box boundaries, and the red and light blue spheres represent argon molecules and carbon atoms, respectively.

of the pressure tensor components and the snapshots for these three systems are shown in Fig. 8.

For $H^* = 15$, although the argon molecules fill up the pore (see the snapshot in Fig. 8(a)) as for smaller pores (Fig. 2 of Ref. 16), only the argon molecules close to the walls are arranged in ordered layers (about two layers on each side), whereas those in the central region are arranged more randomly (i.e., weaker layering effect); this can be compared to the case in smaller pores ($H^* < 8.0$), where almost all the argon molecules are aligned in order across the pore width (Fig. 2 of Ref. 16). In agreement with this adsorbate configuration, the peak tangential pressure is still very high for the contact layers (~18 800 bar), but the local peak of the tangential pressure decays almost exponentially as it

approaches the central region. The normal pressure is constant at ∼27 bar.

For $H^* = 30$, the pore is so large that the argon molecules do not completely fill the pore at the given condition (see the snapshot in Fig. 8(b)). However, the argon molecules close to the walls are still arranged in ordered layers (about two or three layers on each side), and are followed by an intermediate region of condensed argon molecules arranged much more randomly (a liquid-like phase). In the most central region, a gas-like phase (similar to the bulk phase) is present. Hence, due to the large pore width, argon molecules are adsorbed as if there were two separated carbon surfaces. In agreement with this structure, the peak tangential pressure is also very high for the contact layers (∼17 500 bar), and the local peak of the tangential pressure decays rapidly as it approaches the central region. The normal pressure is constant at ∼17 bar. This behavior of the pressures is similar to the case of $H^* = 15$, with greater reduction in pressure enhancement due to the larger pore size.

Bulk argon in a cubic simulation box with side of 8 nm (or 23.5 in reduced units) and periodic boundary conditions applied to each direction behaves similarly as an ideal gas (see the snapshot in Fig. 8(c)). The calculated tangential (parallel to the z-plane) and normal (perpendicular to the z-plane) pressures are ∼1.03 bar and are the same in the whole simulation box within statistical error (Fig. 8(c)).

The results show that the pore width strongly affects the structure of the adsorbate and thus the resulting pressure tensor components. A smaller pore with two walls close to each other induces a very close-packed adsorbate phase and thus a large pressure enhancement effect; as the pore becomes larger the adsorbate in the central region is more randomly arranged, and may even become a gas-like phase, resulting in a reduced pressure enhancement effect.

G. Silica pores

Finally, we show the density and pressure profiles of argon adsorbed in a slit silica pore ($H^* = 3.0$) at 87.3 K and 1 bar bulk pressure (Fig. 9). The normal pressure is constant within the interior of the pore, as expected. However, the tangential pressure of argon in the silica pore is significantly lower than that in the carbon pore of the same slit separation, at the same bulk condition (∼2000 bar compared with 20 000–30 000 bar for the local peak values); thus, the pressure enhancement effect in the silica pore is significantly reduced compared with that in the carbon pore. We also note that, although there are only two adsorbed layers in the carbon pore (Fig. 4(a)), there are five layers of argon molecules adsorbed in the slit silica pore with $H^* = 3.0$ as can been seen from the density profiles (cf. Figs. 9(a) and 9(b)). Moreover, the peak value of the density is appreciably smaller ($\rho^* \sim 2.5$) than in the carbon pore ($\rho^* \sim 8$). From the z-coordinates of the contact layer of argon and of the wall atoms, we see that the contact layer is located at a plane where there are also wall atoms. This results from the fact that the silica wall surface is "atomically rough," so that the adsorbate can be "embedded" into the wall (Fig. 10(a)). The radial distribution function (Fig. 9(c)) shows that in the argon layers,

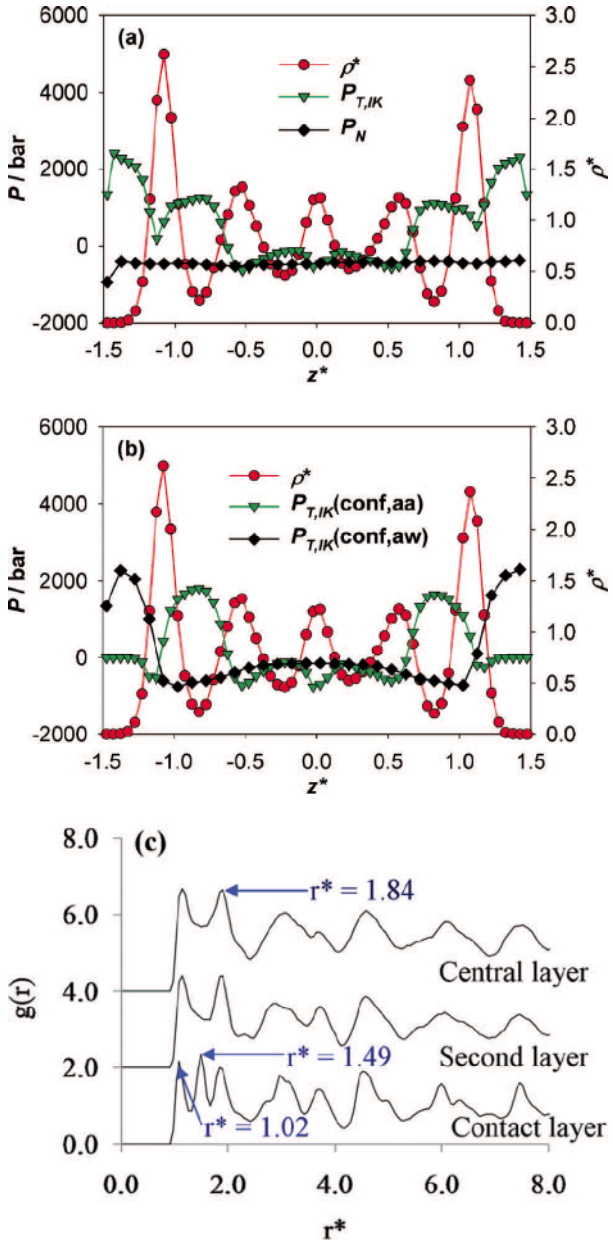

FIG. 9. (a) The density and pressure profiles of argon in the atomistic rigid silica slit-pore model with finite length with $H^* = 3$ at 87.3 K and 1 bar bulk pressure; (b) the individual contributions to the tangential pressure; and (c) the in-plane radial distribution function of the different argon layers.

there are strong peaks located at a separation distance larger than 1.49 (in reduced units), which gives rise to an attractive interaction between adsorbate-adsorbate molecules, and results in a negative adsorbate-adsorbate configurational contribution to the tangential pressure (Fig. 9(b)) at the planes where there are argon layers.

In the silica pore (or any pore with rough surface), the separation distance between neighboring argon molecules in the contact layer is dominated by surface geometric effects: as adsorption starts, the adsorbate molecule tends to be accommodated on the wall surface or the "hole" of a rough surface where the attractive interaction is the strongest (Fig. 10(a)), instead of being closely packed as on a smooth surface or

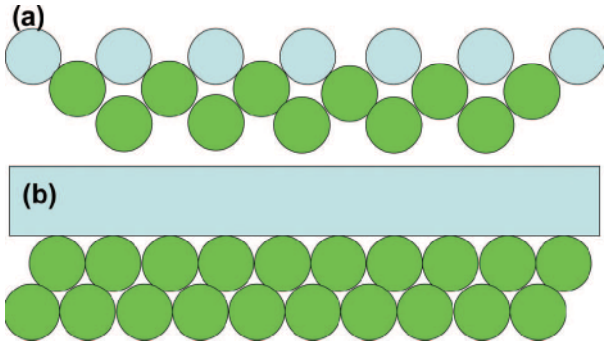

FIG. 10. Schematic representations of adsorbate molecules accommodated on (a) a rough surface (e.g., the surface of a silica pore) and (b) a smooth surface or an atomistic surface with high atomic density (e.g., the graphene surface). The dark circles (green) represent the adsorbate molecules, and light circles or slab (light blue) represent the wall surface.

atomistic surface with very high surface density (e.g., atomistic graphene) (see Fig. 10(b)). Thus, the distance between neighboring adsorbate molecules on a rough surface strongly depends on the geometric arrangement of the surface atoms. The arrangement of the adsorbate in the contact layer also influences the arrangement of the second layer of adsorbate, which can also be embedded partly in the contact layer; this holds true for the following adsorbate layers as the adsorption progresses. Since the adsorbate layers are partly embedded with each other, their interlayer spacing is smaller than the effective diameter of the adsorbate molecule, thus allowing five layers of argon in a silica pore of $H^* = 3.0$, with lower density peaks.

V. CONCLUSIONS

In summary, our calculations have shown that very high tangential and normal pressures are expected in carbon nanopores with relatively smooth walls. Moreover, these two pressures show distinctly different behaviors, with the local tangential pressure being strongly dependent on the distance from the wall and about an order of magnitude larger than the normal pressure. These in-pore pressures, which are several orders of magnitude larger than their equilibrium bulk counterparts, provide a unifying explanation for a wide range of previously unconnected experimental observations. The pressure enhancement effect arises from the strong attractive nature of the pore wall, which leads to a strong compression of the adsorbate, particularly for molecules in contact with the wall. The compression leads to a strong repulsive force between adsorbate molecules (especially in the tangential direction); thus, a relatively small change in the in-pore density, resulting from a correspondingly small change in the equilibrium bulk pressure, has a very large effect on the in-pore tangential pressure. This suggests that it should be possible to experimentally observe a range of high-pressure phenomena by simply varying the bulk pressure. The pressures calculated from the mechanical and the thermodynamic routes yield identical results to within the measurable error, suggesting that both methods can be equivalently used to calculate the local pressure tensor component. The thermodynamic route[30] could be useful to calculate the pressure tensor for pores of other geometries, where the corresponding formulae with the mechanical route have not yet been derived.[32] The in-pore pressure is very sensitive to the roughness of the wall surface, as the pressure enhancement effect relies on the ability to form well-defined layers of adsorbate. A rough surface geometry impedes the compression of the fluids, particularly in the contact layers.

Finally, we note that large tangential pressures are not unexpected even for fluid-fluid interfaces. Thus, the interfacial tension, γ, of a planar interface can be obtained from the mechanical definition, $\gamma = \int_{-\infty}^{\infty} (P_N - P_T(z))\, dz$. For the vapor-liquid interface of water at 25 °C, the surface tension is 75 mN m^{-1} and $P_N = P_{bulk} = 0.03$ bar. This means that for a typical interfacial width of $w = 1$ nm, the average $\langle P_N - P_T(z) \rangle = 7.5 \times 10^7$N m^{-2} = 750 bar. As the bulk pressure is small, the average tangential pressure, $\langle P_T(z) \rangle \sim -750$ bar, a large negative value. As shown in this paper, the effect is amplified in the case of nano-phases confined between solid surfaces, and the tangential pressure is positive rather than negative as a result of the lateral compression of molecules near the wall due to the strongly attractive wall forces.

ACKNOWLEDGMENTS

We thank the National Science Foundation (Grant No. CBET-1160151) for support of this research. Computational time was provided through a Teragrid Research Allocation by the U.S. National Science Foundation (Grant No. CHE080046N). G.J. and E.A.M. gratefully acknowledge further support to the MSE group from the Engineering and Physical Sciences Research Council (EPSRC) of the UK (Grant Nos. EP/E016340 and EP/J014958).

[1] O. Byl, P. Kondratyuk, and J. T. Yates, J. Phys. Chem. B **107**, 4277–4279 (2003).
[2] H. W. Hu, G. A. Carson, and S. Granick, Phys. Rev. Lett. **66**, 2758–2761 (1991).
[3] K. Kaneko, N. Fukuzaki, K. Kakei, T. Suzuki, and S. Ozeki, Langmuir **5**, 960–965 (1989).
[4] J. Klein and E. Kumacheva, Science **269**, 816–819 (1995).
[5] J. Klein and E. Kumacheva, J. Chem. Phys. **108**, 6996–7009 (1998).
[6] E. Kumacheva and J. Klein, J. Chem. Phys. **108**, 7010–7022 (1998).
[7] K. Urita, Y. Shiga, T. Fujimori, T. Iiyama, Y. Hattori, H. Kanoh, T. Ohba, H. Tanaka, M. Yudasaka, S. Iijima, I. Moriguchi, F. Okino, M. Endo, and K. Kaneko, J. Am. Chem. Soc. **133**, 10344–10347 (2011).
[8] B. Coasne, J. Czwartos, M. Sliwinska-Bartkowiak, and K. E. Gubbins, J. Phys. Chem. B **113**, 13874–13881 (2009).
[9] Y. Fujiwara, K. Nishikawa, T. Iijima, and K. Kaneko, J. Chem. Soc., Faraday Trans. **87**, 2763–2768 (1991).
[10] K. Kaneko, Y. Fujiwara, and K. Nishikawa, J. Colloid Interface Sci. **127**, 298–299 (1989).
[11] K. Kaneko, T. Suzuki, Y. Fujiwara, and K. Nishikawa, *Proceeding Invited Papers, Characterization of Porous Solids II, Alacant, 1990* (Elsevier Science, Amsterndam, 1991), pp. 389–398.
[12] T. Suzuki and K. Kaneko, Carbon **26**, 744–745 (1988).
[13] G. Gunther, J. Prass, O. Paris, and M. Schoen, Phys. Rev. Lett. **101**, 086104 (2008).
[14] G. Gunther and M. Schoen, Phys. Chem. Chem. Phys. **11**, 9082–9092 (2009).
[15] Y. Long, J. C. Palmer, B. Coasne, M. Śliwinska-Bartkowiak, and K. E. Gubbins, Microporous Mesoporous Mater. **154**, 19–23 (2012).
[16] Y. Long, J. C. Palmer, B. Coasne, M. Śliwinska-Bartkowiak, and K. E. Gubbins, Phys. Chem. Chem. Phys. **13**, 17163–17170 (2011).
[17] J. H. Irving and J. G. Kirkwood, J. Chem. Phys. **18**, 817–829 (1950).

[18]C. G. Gray, K. E. Gubbins, and C. G. Joslin, *Theory of Molecular Fluids, Vol. 2: Applications* (Oxford University Press, Oxford, 2011), pp. 928–942.
[19]J. S. Rowlinson and B. Widom, *Molecular Theory of Capillarity* (Clarendon Press, Oxford, 1982).
[20]P. Schofield and J. R. Henderson, Proc. R. Soc. London **379**, 231–246 (1982).
[21]J. P. R. B. Walton, D. J. Tildesley, J. S. Rowlinson, and J. R. Henderson, Mol. Phys. **48**, 1357–1368 (1983).
[22]A. Harasima, Adv. Chem. Phys. **1**, 203–237 (1958).
[23]R. Eppenga and D. Frenkel, Mol. Phys. **52**, 1303–1334 (1984).
[24]V. I. Harismiadis, J. Vorholz, and A. Z. Panagiotopoulos, J. Chem. Phys. **105**, 8469–8470 (1996).
[25]H. L. Vortler and W. R. Smith, J. Chem. Phys. **112**, 5168–5174 (2000).
[26]E. de Miguel and G. Jackson, Mol. Phys. **104**, 3717–3734 (2006).
[27]E. de Miguel and G. Jackson, J. Chem. Phys. **125**, 164109 (2006).
[28]A. Botan, B. Rotenberg, V. Marry, P. Turq, and B. Noetinger, J. Phys. Chem. C **114**, 14962–14969 (2010).
[29]P. E. Brumby, A. J. Haslam, E. de Miguel, and G. Jackson, Mol. Phys. **109**, 169–189 (2011).
[30]G. J. Gloor, G. Jackson, F. J. Blas, and E. de Miguel, J. Chem. Phys. **123**, 134703 (2005).
[31]A. Ghoufi, F. Goujon, V. Lachet, and P. Malfreyt, J. Chem. Phys. **128**, 154716 (2008).
[32]J. G. Sampayo, A. Malijevsky, E. A. Muller, E. de Miguel, and G. Jackson, J. Chem. Phys. **132**, 141101 (2010).
[33]A. Ghoufi, F. Goujon, V. Lachet, and P. Malfreyt, Phys. Rev. E **77**, 031601 (2008).
[34]A. Ghoufi and P. Malfreyt, J. Chem. Phys. **135**, 104105 (2011).
[35]A. Ghoufi and P. Malfreyt, J. Chem. Phys. **136**, 024104 (2012).
[36]C. Ibergay, A. Ghoufi, F. Goujon, P. Ungerer, A. Boutin, B. Rousseau, and P. Malfreyt, Phys. Rev. E **75**, 051602 (2007).
[37]A. J. C. Ladd and L. V. Woodcock, Mol. Phys. **36**, 611–619 (1978).
[38]C. R. Fuselier, J. C. Raich, and N. S. Gillis, Surf. Sci. **92**, 667–680 (1980).
[39]J. A. Barker, R. A. Fisher, and R. O. Watts, Mol. Phys. **21**, 657 (1971).
[40]M. J. McGrath, J. N. Ghogomu, N. T. Tsona, J. I. Siepmann, B. Chen, I. Napari, and H. Vehkamaki, J. Chem. Phys. **133**, 084106 (2010).
[41]W. A. Steele, Surf. Sci. **36**, 317–352 (1973).
[42]S. J. Stuart, A. B. Tutein, and J. A. Harrison, J. Chem. Phys. **112**, 6472–6486 (2000).
[43]J. D. Weeks, D. Chandler, and H. C. Andersen, J. Chem. Phys. **54**, 5237 (1971).
[44]F. Liu, S. H. Garofalini, R. D. Kingsmith, and D. Vanderbilt, Phys. Rev. Lett. **70**, 2750–2753 (1993).
[45]R. J. M. Pellenq and D. Nicholson, J. Phys. Chem. **98**, 13339–13349 (1994).
[46]R. J. M. Pellenq and P. E. Levitz, Mol. Phys. **100**, 2059–2077 (2002).
[47]J. Jagiello and J. P. Olivier, J. Phys. Chem. C **113**, 19382–19385 (2009).
[48]R. Radhakrishnan, K. E. Gubbins, and M. Sliwinska-Bartkowiak, J. Chem. Phys. **112**, 11048–11057 (2000).
[49]R. Radhakrishnan, K. E. Gubbins, and M. Sliwinska-Bartkowiak, J. Chem. Phys. **116**, 1147–1155 (2002).
[50]S. T. Cui, C. McCabe, P. T. Cummings, and H. D. Cochran, J. Chem. Phys. **118**, 8941–8944 (2003).